Construction and Building Materials 304 (2021) 124436

Contents lists available at ScienceDirect

Construction and Building Materials

journal homepage: www.elsevier.com/locate/conbuildmat

Towards a more effective and reliable salt crystallisation test for porous building materials: Predictive modelling of sodium chloride salt distribution

Antonio Maria D'Altri [a], Stefano de Miranda [a], Kevin Beck [b], Tim De Kock [c,d], Hannelore Derluyn [e,*]

[a] Department of Civil, Chemical, Environmental, and Materials Engineering (DICAM), University of Bologna, Viale del Risorgimento 2, Bologna 40136, Italy
[b] Univ. Orleans, Univ. Tours, INSA-CVL, LaMé EA7494, 8 rue Léonard de Vinci, F-45072 Orleans, France
[c] University of Antwerp, Antwerp Cultural Heritage Sciences, Faculty of Design Sciences, Mutsaardstraat 31, 2000 Antwerpen, Belgium
[d] Ghent University, PProGRess-UGCT, Krijgslaan 281/S8, 9000 Ghent, Belgium
[e] Universite de Pau et des Pays de l'Adour, E2S UPPA, CNRS, Total, LFCR UMR5150, Pau, France

ARTICLE INFO

Keywords:
Salt crystallisation
Building stones
Salt accumulation
Multiphase modelling
Finite element method

ABSTRACT

The RILEM TC ASC-271 is designing a new procedure to assess the durability of porous building materials to salt crystallisation in the laboratory, consisting of a salt accumulation and a damage propagation phase. The salt accumulation consists of the capillary absorption of a salt solution followed by drying at low humidity to crystallize salts close to the evaporative surface without inducing damage. This was experimentally verified on Maastricht and Migné limestone but poses the question of whether the accumulation procedure can be extrapolated to other porous building materials and if the salt distribution is influenced by the salt concentration and drying conditions. Using a multiphase numerical model, sodium chloride accumulation can be accurately predicted for both stones. Furthermore, numerical simulations confirm that the protocol remains valid for other porous building materials and while moderately varying the concentration of the absorbed salt solution and the relative humidity while drying. Consequently, the protocol's general applicability is confirmed, proving its suitability for developing a more effective salt crystallization test.

1. Introduction

Salt weathering is a major problem for the durability of porous building materials and plays a significant role in the conservation of historical monuments and our cultural heritage, as well as in the life span of construction materials (e.g. [1–3]). In order to assess the durability of building materials to salt weathering, accelerated laboratory tests are carried out. The RILEM Technical Committee (TC) ASC-271 ("Accelerated laboratory test for the assessment of the durability of materials with respect to salt crystallization"), launched in 2016, published two state of the art review articles on this subject. They focus on laboratory salt crystallization tests for porous building materials [4] and the associated theoretical principles [5], including salt transport mechanisms, the conditions of exposure, and the chemo-mechanics of crystallization pressure resulting in damage [6–9]. There are several standards and guidelines to test the durability of building materials to salt crystallization, although no common test protocol is well accepted to date by the scientific community. This makes practitioners and researchers modify existing procedures, leading to incomparable results.

The aim of the TC ASC-271 is to develop an accelerated salt weathering test that represents deterioration mechanisms occurring onsite. Salt spray tests are generally well accepted and effective in reproducing onsite damage mechanisms [10,11], so they are not included in this study. The TC ASC-271 focuses on salt damage induced by salt transport towards the evaporative surface of a building material. A new test protocol is currently under development, consisting of two distinct phases [5]: (1) the accumulation phase, during which the pore space gets filled by salt crystals, without damaging the solid material, and

* Corresponding author at: Université de Pau et des Pays de l'Adour, LFCR - UMR 5150, DMEX - Halle Technologique Collège STEE, Avenue de l'Université, 64000 Pau, France.
E-mail addresses: am.daltri@unibo.it (A.M. D'Altri), stefano.demiranda@unibo.it (S. de Miranda), kevin.beck@univ-orleans.fr (K. Beck), tim.dekock@uantwerpen.be (T. De Kock), hannelore.derluyn@univ-pau.fr (H. Derluyn).

https://doi.org/10.1016/j.conbuildmat.2021.124436
Received 21 December 2020; Received in revised form 17 July 2021; Accepted 2 August 2021

without or with limited formation of efflorescence, and (2) the propagation phase, during which weathering cycles lead to damage initiation and propagation. During the accumulation phase, salt should precipitate in a thin layer close to the evaporative surface to create a localized accumulation zone, as this is the most common situation found onsite. Water transport properties, governed by the pore structure of the material, and crystallization kinetics will control the salt distribution in the accumulation phase [12–15]. In the propagation phase, also the mechanical properties of the material and the environmental conditions will play an important role in the eventual damage mechanism [1,5,16,17]. By clearly separating between a salt accumulation and a damage propagation phase, the test procedure distinguishes itself from existing salt weathering tests. The main novelty is to be able to define the risk for salt damage due to dissolution-crystallization cycles, depending on the salt content and the corresponding degree of pore filling accumulated in the first phase. This idea originates from the expression for the resulting macroscopic tensile stress σ^* due to in-pore crystallization [5]:

$$\sigma^* = bS_c p_c \tag{1}$$

where b is the Biot's coefficient, i.e. a material property, S_c is the volume fraction of the porous network filled with crystals, and p_c is the crystallization pressure. When the macroscopic tensile stress exceeds a failure criterion, damage is initiated. The salt accumulation phase is reflected in the expression above by the term S_c, whereas the start of the propagation phase will be controlled by the crystallization pressure p_c and the resulting tensile stress σ^*.

In the first step of the design of the new salt weathering test, the TC ASC-271 focuses on the salt accumulation phase. The experimental salt accumulation procedure is described by Nunes et al. [18] and is based on tests performed on two stones, Maastricht and Migné limestone, with single salt solutions of sodium chloride and sodium sulphate. Nunes et al. conclude that the best accumulation procedure consists of one wetting step with a salt solution of a predefined concentration, followed by one unidirectional drying step at a controlled constant relative humidity and temperature. This conclusion is based on an extensive characterization of the salt distribution by comparing results obtained via several experimental techniques (ultrasonic pulse velocity, hygroscopic moisture content, ion chromatography, scanning electron microscopy, micro X-ray fluorescence mapping, drilling resistance method and scratch test) [18]. The question remains however if the procedure, tested on two stones, can be extrapolated to other porous building stones, and if the salt distribution is influenced by the choice of salt concentration and drying conditions. To answer this question, numerical modelling can complement experimental testing, by varying parameters and testing in silico the material response.

To assist the TC ASC-271 in its decision process, a multiphase numerical model is employed in the study at hand to solve the mass balance equations for the coupled multiphase problem of salt transport and crystallization (as also pursued by akin numerical models, see e.g. [19–21]). The particularity of this model, which follows the developments in [22,23], is the incorporation of a phenomenological description of salt efflorescence, where all efflorescence is lumped in the boundary element of the finite element mesh. Efflorescence is not modelled explicitly, as the salt cannot grow outside of the initial model domain. As such, no discrimination is made between pore filling on the border and efflorescence itself, but the phenomenological description allows correctly reproducing the drying kinetics when efflorescence affects the drying rate. The model has been experimentally validated for sodium chloride precipitation under isothermal conditions [23]. The numerical study will therefore focus on the salt accumulation procedure with sodium chloride. The numerical modelling of sodium sulphate accumulation, which requires to include and to validate the potential precipitation of the different crystal phases of sodium sulphate, is the subject of future work.

The aim of the work presented in this paper is to determine (i) if the accumulation procedure, designed by the experimental testing on two limestones [18], is generally applicable, and (ii) how sensitive this procedure is to the salt solution concentration and the imposed drying conditions. Accordingly, a characterization of the physical, moisture transport and mechanical properties needed as input for numerical modelling is performed on Maastricht and Migné limestone. The numerical model is validated against experimental results on the drying kinetics, presented in this paper, and on the salt distributions obtained by Nunes et al [18]. The model is then further exploited for other porous building materials, considering also variations of the salt concentration and of the relative humidity during drying. The damage propagation phase is not treated in the current study, but will be the subject of future publications by the RILEM TC ASC-271.

2. Materials characterization and experimental results on sodium chloride salt accumulation

2.1. Maastricht and Migné limestone

Maastricht and Migné stone have been selected to develop the RILEM-TC ASC-271 test procedure. Both stones are sedimentary porous limestones. Maastricht stone is a yellowish limestone extracted in the Netherlands, and Migné stone is a white limestone extracted in France. Both stones are composed mainly of calcite, with a small amount of quartz in the case of Maastricht stone. These stones were selected because of their homogeneous structure with a unimodal pore size distribution. The major differences between them are the porosity and the size of the main pores.

The key properties for this study were determined by laboratory testing of stone samples. The results for the physical, mechanical and water transport properties of the two selected stones are summarised in Table 1. The dry bulk density, specific gravity, total open porosity and mean pore size were measured on three samples of about 1 cm^3 by mercury intrusion porosimetry (MIP) using an Autopore IV9520 microporosimeter operated in the range of 2.76 kPa to 414 kPa. The capillary test was carried out according to the standard EN 1925 (1999) [24] on three drill cores of each stone type (diameter: 40 mm, height: 80 mm). Mechanical measurements were performed on stones in their dry state, after drying in an oven at 70 °C until constant weight and cooling in a desiccator. The uniaxial compressive strength (UCS) was measured according to the standard P94-420 [25] on three specimens of each stone type (diameter: 40 mm, height: 80 mm). The tensile strength was measured according to the Brazilian test, also on three specimens of each stone type (diameter: 40 mm, height: 40 mm), by applying a compressive load diametrically on the circular cross-section of the cylindrical specimen according to the standard P94-422 [26].

Fig. 1 presents the microstructure of both stones with images obtained by Scanning Electron Microscopy (SEM) and their pore size distribution obtained by MIP. Fig. 2 presents their complete water retention

Table 1
Properties of the two selected stones.

	Maastricht stone	Migné Stone
Dry bulk density (g/cm^3)	1.26 ± 0.01	1.81 ± 0.02
Specific gravity (g/cm^3)	2.69 ± 0.01	2.68 ± 0.02
Total open porosity (%)	53.1 ± 0.4	32.4 ± 0.5
Mean pore diameter (Hg volume) (μm)	30.4 ± 0.2	0.95 ± 0.05
Water uptake capillary coefficient A_{cap} ($g/cm^2/min^{0.5}$)	2.19 ± 0.16	0.23 ± 0.01
Wetting front capillary coefficient ($cm/min^{0.5}$)	4.92 ± 0.09	0.93 ± 0.02
Degree of saturation by capillary absorption (%)	77.6 ± 0.5	83.0 ± 1.1
Uniaxial compressive strength (MPa)	1.95 ± 0.14	12.26 ± 1.76
Tensile strength – Brazilian test (MPa)	0.25 ± 0.01	1.11 ± 0.24

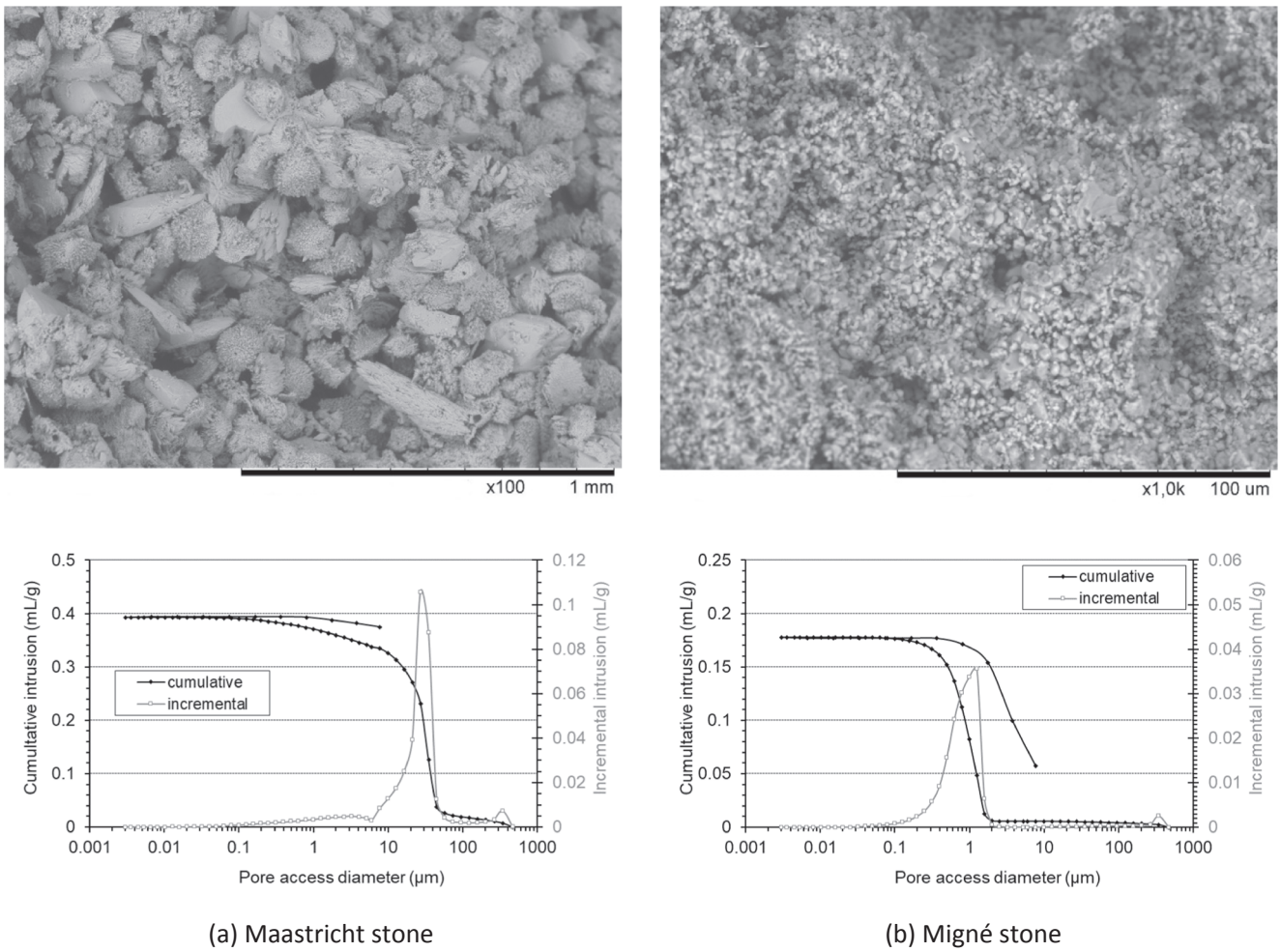

Fig. 1. Microstructure by SEM images and pore size distribution by MIP for the two selected stones: (a) Maastricht stone, (b) Migné stone.

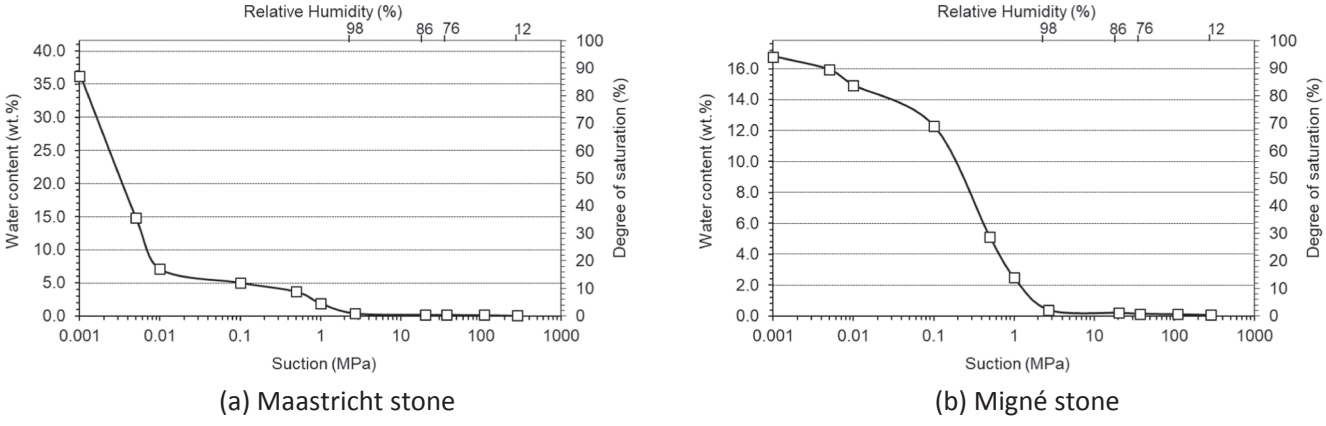

Fig. 2. Water retention curves for the two selected stones: (a) Maastricht stone, (b) Migné stone.

curve in the capillary saturation regime. In this test, three dry stone samples of about 3 cm^3 were put in contact with systems imposing water suction (atmosphere with constant relative humidity for high suctions, PEG osmotic solution across a semi permeable membrane for intermediate suctions, tensiometric plates for low suctions) [27]. At equilibrium, i.e. when reaching a constant weight, the water content of the stone samples was measured, and the associated degree of saturation was calculated.

Both Migné stone and Maastricht stone have a high porosity according to the classification developed by Von Moos and De Quervain with a significantly high amount of pore space [28]. The porosity of Migné stone is about 30%, and the porosity of Maastricht stone is more than 50%, which makes the latter a very light building stone with a dry bulk density close to 1.2 g/cm^3. The specific gravities are close for the two stones, with a value of 2.69 g/cm^3, and close to the value of the density of calcite (Table 1). The grain sizes are very homogeneous for both stones, but very different in order of magnitude. Indeed, the grain sizes are about 100–150 μm for Maastricht stone and about 1–5 μm for

Migné stone, as estimated from the SEM images. That is why both limestones have a unimodal pore size distribution, with a mean pore diameter of around 30 μm for Maastricht stone, which has the coarsest grains, and a mean pore diameter of around 1 μm for Migné stone, which has the finest grains (Fig. 1). Even if Maastricht limestone has very coarse pores, all the pores are still in the range of capillary pores (<1mm) [28]. The difference in pore sizes causes a great difference in capillary water absorption. Indeed, the wetting front capillary coefficient is 5 times higher for Maastricht stone compared to Migné stone. Only 2 minutes are needed to wet by capillarity a height of 50 mm of Maastricht stone compared to 30 minutes for Migné stone. The water uptake capillary coefficient A_{cap} is 10 times higher for Maastricht stone, as its porosity is about 2 times higher than the porosity of Migné stone. At the end of capillary imbibition, both stones are not fully saturated, as they only attain a degree of saturation of around 80%. For the water retention curve, the standard deviation of each measured point is very low because the two stones are very homogeneous. Both stones have no hygroscopic behaviour as the water retention curves (Fig. 2) show water contents lower than 1% for high values of suction (i.e. for relative humidity values lower than 98%). Consequently, these stones are often nearly dry given the relative humidity values of the atmosphere in Europe. For lower suction, both stones present a water percolating behaviour with a high increase of water content for a given value of suction. This behaviour is directly linked to the unimodal pore size distribution of the two stones. Maastricht stone has coarser pores compared to Migné stone, and so, the increase of water content takes place at a lower suction value. Both stones are soft building stones. Values of uniaxial compressive strengths in their dry state are around 2 MPa for Maastricht stone and 12 MPa for Migné stone, i.e. Maastricht stone is six times weaker than Migné stone. Indirect tensile strengths, measured by the Brazilian splitting test, represent around 10% of the compressive strength.

To assess the diffusivity for water, D_w, of both stones, the methodology as described by Carmeliet et al. [29] and Roels et al. [30] was employed. To this extent, capillary water uptake was visualized by means of X-ray radiography in the HECTOR scanner [31] of the Ghent University Centre for X-ray Tomography on samples of 10 mm thickness, 50 mm in width and 100 mm in height. For each stone, a dry sample was positioned in the X-ray scanner just above the water level of a water basin. Water was then remotely injected into the basin until a permanent contact with the bottom surface was established, while acquiring radiographs continuously with an exposure time of 1 s at an energy of 160 keV and a tube voltage of 10 W. A filter of 0.5 mm aluminium was placed in front of the source to filter the low energy photons out of the polychromatic X-ray spectrum in order to avoid beam-hardening artefacts. By applying the Boltzmann transformation method, the water diffusivity was calculated from the moisture content profiles derived from the X-ray radiography series (Fig. 3).

The logarithm of the water diffusivity is typically approximated by a linear function [29,32]. Here, we employ:

$$\log D_w = \log\left(F_1\left(\frac{A_{cap}}{\phi_0\rho_w^l}\right)^2\right) + F_2\left(S_w^l - 1\right) \quad (2)$$

where $F_1\left(\frac{A_{cap}}{\phi_0\rho_w^l}\right)^2$ is the water diffusivity when the sample is capillary saturated with water, i.e. when the capillary water saturation degree S_w^l equals 1. ρ_w^l is the liquid water density, and ϕ_0 the capillary active porosity, i.e. the total open porosity multiplied with the degree of saturation by capillary absorption. Thus, Maastricht has a capillary active porosity of ± 42% and Migné of ± 27%. The parameter F_1 equals 0.28 for Maastricht and 0.6 for Migné, whereas the parameter F_2 equals 1.7 for both stones.

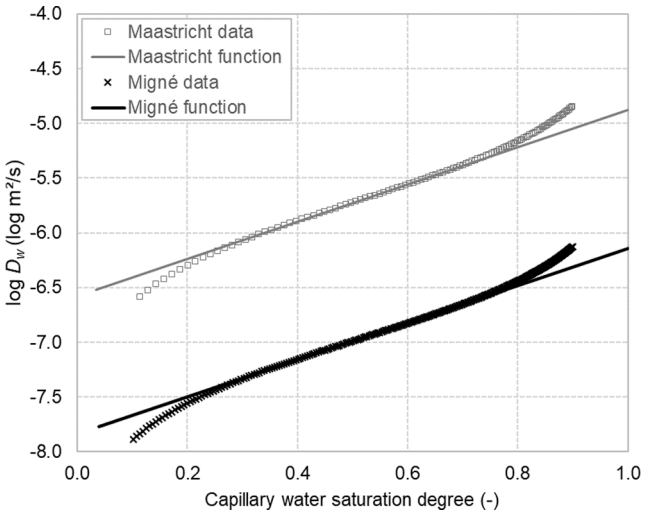

Fig. 3. Water diffusivity $D_w$as a function of capillary water saturation degree for Maastricht and Migné limestone.

2.2. Sodium chloride salt accumulation in Maastricht and Migné limestone

The salt accumulation procedure considered in this paper is the procedure P1-1S retained by Nunes et al. [18]. This paper will furthermore focus on the accumulation of NaCl, the accumulation of Na_2SO_4, with its complexity of the formation of hydrated and anhydrous crystal phases, will be the subject of future numerical studies. Procedure P1-1S proved to be the fastest and most effective procedure for accumulating salt in a thin layer of material close to the evaporative surface, without resulting in too much efflorescence or damage. This procedure consists in capillary saturating a sample that has been sealed along its side surface, by capillary absorption of a salt solution through its bottom surface. This bottom surface is subsequently sealed, and the sample is put in a conditioned environment to dry via its top surface only. The procedure is limited to one wetting-by-absorption step and one drying step.

The RILEM-TC ASC-271 applied this procedure on cylindrical samples of 5 cm in diameter and 5 cm in height of Maastricht and Migné limestone [18]. The samples were capillary saturated with a salt concentration corresponding to a salt amount of 1 wt% of the dry weight of the sample. This corresponds to a salt solution concentration of 6.7 wt% (mass of dissolved salt per unit mass of liquid solution) for Migné, and 3.8 wt% for Maastricht limestone. The samples were then dried in a climatic chamber, aiming for constant drying conditions of 20°C and 10% RH, and minimizing the air flow around the samples.

Samples were tested at two different laboratories, experimental series 1 at the Institute of Theoretical and Applied Mechanics of the Czech Academy of Sciences, and experimental series 2 at the Geosciences and Environment Cergy Laboratory. The weight loss during drying was monitored until at least 80% of the water content evaporated. Experimental series 1 consists of drying curves with pure water and with salt solution, whereas experimental series 2 only includes drying curves with salt solution. The data points shown in Fig. 4 show the mean and standard deviation of a group of 3 samples for each test in experimental series 1 and a group of 12 samples for each test in experimental series 2.

As expected, the drying rate of a sample saturated with pure water is faster than for a sample saturated with salt solution. For Migné stone, the drying curves with salt solution give similar results at both laboratories, whereas for Maastricht stone, there is a significant difference. The climatic conditions reported at both laboratories were a temperature of 20 °C and a relative humidity varying between 10 and 15%.

The salt distribution assessments performed by Nunes et al. [18] revealed that most of the salt accumulates in the first few millimeters below the evaporative surface, and mostly in the first 1 to 2 mm. In

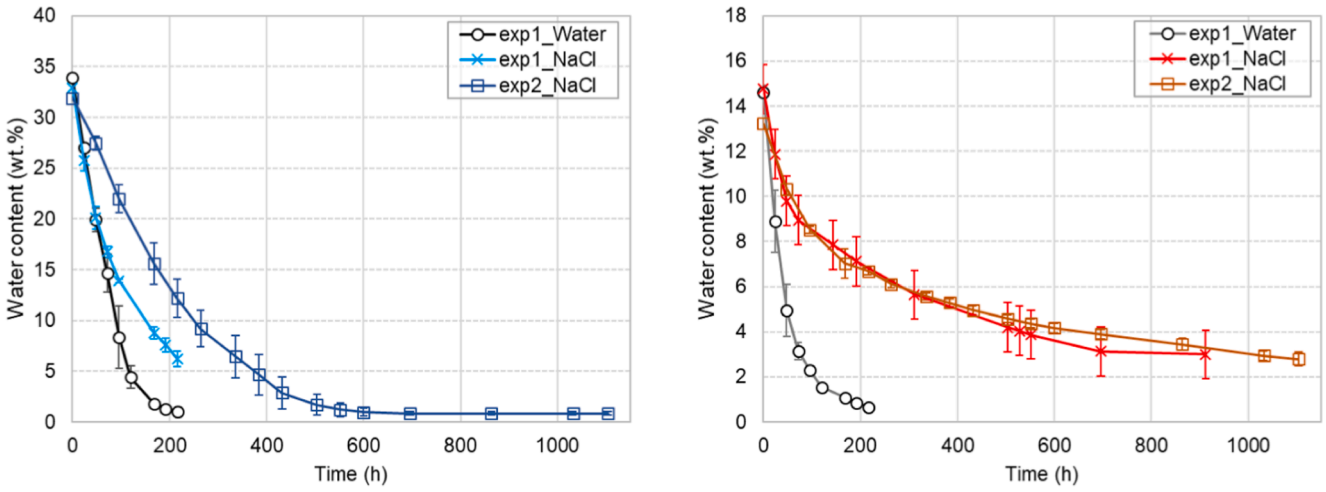

Fig. 4. Drying curves for Maastricht and Migné stone during the salt accumulation procedure.

addition, salt efflorescence was described for the experimental series 1. For the Migné stone this efflorescence is limited and amounts to 5.9% of the total precipitated salt mass amount, consisting of a thin layer of powdery salt efflorescence. On the other hand, for Maastricht stone, the salt efflorescence accounts for more than 20% of the total salt mass and consists of well-adhered cauliflower-shaped efflorescence. As Maastricht stone has a much higher capillary absorption coefficient and water diffusivity than Migné limestone, more efflorescence is an expected outcome as transport to the evaporating surface is enhanced.

Salt efflorescence impacts the drying behaviour, which might explain the larger discrepancy between the Maastricht datasets if variations in the resulting efflorescence occurred. The formation of patchy or crusty efflorescence depends on the characteristics of the porous medium, for example its pore size [33], and on the environmental conditions [34,35]. Patchy efflorescence leaves the pore space open, whereas crusty efflorescence blocks the pores and slows down drying. When working at the same environmental conditions, a medium with large pores is more prone to develop patchy efflorescence, while a medium with smaller pores rather develops crusty efflorescence [33]. Additionally, slower drying was observed for the same porous medium when drying at lower relative humidity due to the formation of crusty efflorescence [34,35], while a more patchy efflorescence formed at higher relative humidity.

As the amount of efflorescence for Migné is rather limited, we can assume that subflorescence and thus pore clogging will play a larger role in reducing the drying rate. For Maastricht, however, crusty efflorescence might develop while drying at the low relative humidity defined in the procedure, and small variations in the climatic conditions between experimental series 1 and 2 could explain the difference in the drying curves for Maastricht.

3. Numerical modelling of salt accumulation

In this section, the multiphase model based on the finite element method (FEM) used for salt crystallization simulations in porous media is described (Section 3.1) and validated (Section 3.2) against the experimental campaign summarized in Section 2.2.

3.1. A multiphase FEM model for salt crystallization

The multiphase FEM model adopted to reproduce salt accumulation in natural building stones is herein described. This model has been initially developed in [22] for masonry walls exposed to salt attack, and a brief recall of the model equations is given below. According to the model in [22], the porous material is treated as a multiphase continuous porous medium composed of the material matrix (solid phase), water (gaseous and/or liquid phase), and salt (liquid and/or solid phase). The concentration c_α^π (mass of the species α in phase π, m_α^π, per unit volume of the medium) and the saturation degree S_α^π (pore volume filled by the species α in π-phase) describe the content of each component within the porous medium. Particularly, the pore volume filled by solid salt S_s^s corresponds to the pore filling with respect to the capillary porosity.

The hypotheses of (i) isothermal conditions, (ii) presence of only one salt solid phase, and (iii) concentration of liquid water equal to the concentration of moisture are adopted to simulate the salt accumulation procedure described in the previous section. Accordingly, the multiphase model is described through two balance equations, i.e. the moisture mass conservation equation (3) and the salt mass conservation equation (4), as well as an evolution equation (8) defining the kinetics of salt precipitation/dissolution. The model is formulated in terms of three independent variables, i.e. the pore relative humidity h (ratio between the actual vapor pressure and the vapor pressure at saturation), the mass fraction of the dissolved salt ω, and the concentration of crystallized salt c_s^s.

Firstly, imposing moisture mass conservation leads to:

$$\frac{\partial c_w}{\partial t} + \nabla \bullet \mathbf{j}_w = 0 \tag{3}$$

being c_w the concentration of moisture, $\mathbf{j}_w$ the water flux ($\mathbf{j}_w = \mathbf{j}_w^g + \mathbf{j}_w^l$, where $\mathbf{j}_w^g$ is the water vapor flux and $\mathbf{j}_w^l$ the water liquid flux), and $\frac{\partial}{\partial t}$ the time derivative.

Secondly, imposing salt mass conservation leads to:

$$\frac{\partial c_s^l}{\partial t} + \nabla \bullet \mathbf{j}_s^l + \frac{\partial c_s^s}{\partial t} = 0 \tag{4}$$

being $\mathbf{j}_s^l$ the flux of dissolved salt and c_s^l the concentration of dissolved salt. The fluxes $\mathbf{j}_w^l$ and $\mathbf{j}_s^l$ can be expressed as follows:

$$\mathbf{j}_w^l = (1-\omega)\mathbf{j}_{ws}^l - \mathbf{j}_{s,diff}^l \tag{5}$$

$$\mathbf{j}_s^l = \omega \mathbf{j}_{ws}^l + \mathbf{j}_{s,diff}^l \tag{6}$$

being $\mathbf{j}_{ws}^l$ the flux of the liquid phase and $\mathbf{j}_{s,diff}^l$ the diffusive flux of the dissolved salt.

Thirdly, the supersaturation ratio ω/ω_{sat} (ω_{sat} is the mass of dissolved salt per unit mass of liquid phase at saturation) is assumed to rule the evolution equation, i.e. crystallization occurs when ω/ω_{sat} overtakes the

threshold α_0 and dissolution occurs when ω/ω_{sat} is less than one:

$$\begin{cases} \dfrac{\omega}{\omega_{sat}} > \alpha_0 \Rightarrow crystallization \\ \dfrac{\omega}{\omega_{sat}} < 1 \Rightarrow dissolution \end{cases} \tag{7}$$

Therefore, the evolution equation can be expressed as:

$$\frac{\partial c_s^s}{\partial t} = \pi r_p^2 \rho_s^s \frac{n}{V_{tot}} K_c \left| \frac{\omega}{\omega_{sat}} - 1 \right|^P \tag{8}$$

hypothesizing an isotropic distribution of cylindrical pores, cylindrical nuclei of the same radius of the pores (r_p), and a constant amount of salt nuclei n in the solution. In (8), ρ_s^s is the solid salt density, K_c is the growth rate coefficient, V_{tot} the pore volume, and P is the order of the crystallization process.

The water vapor flux, the capillary liquid flux and the diffusive flux of dissolved salt are defined through the following constitutive relationships:

$$\mathbf{j}_w^g = -K_g \nabla p_v \tag{9}$$

$$\mathbf{j}_{ws}^l = -K_l \nabla p_c \tag{10}$$

$$\mathbf{j}_{s,diff}^l = -\rho_{ws}^l K_s \nabla \omega \tag{11}$$

being K_g the vapor permeability, K_l the liquid permeability of the salt solution, K_s the salt diffusion coefficient, p_v the vapor pressure, p_c the capillary pressure, and ρ_{ws}^l the mass density of the liquid phase.

The vapor permeability K_g can be expressed as:

$$K_g = \frac{D_v}{R_v T} \tag{12}$$

being D_v the vapor diffusivity, R_v the gas constant of water vapor (0.4615 kJ/kg/K) and T the temperature.

The liquid permeability of the salt solution K_l can be written as:

$$K_l = g_\omega K_w f_l(S_w^l) \tag{13}$$

being K_w the liquid permeability for pure water, $f_l(S_w^l)$ a correction function depending on the water saturation degree (here we take $f_l(S_w^l) = S_w^l$), accounting for the fact that liquid flow is no longer possible at low values of the water saturation degree, and g_ω a correction function which accounts for the presence of salt in the solution. The term K_w is herein computed following the expression proposed in [32] and equation (2), i.e.:

$$K_w = D_w \frac{\partial c_w}{\partial p_c} = \frac{h}{\rho_w^l R_v T} \left[F_1 \left(\frac{A_{cap}}{\phi_0 \rho_w^l} \right)^2 10^{F_2 (S_w^l - 1)} \right] \frac{\partial c_w}{\partial h} \tag{14}$$

where A_{cap} is the capillary absorption coefficient of the material, F_1 and F_2 two coefficients experimentally calibrated, and ϕ_0 is the capillary active porosity of the material (as determined in section 2.1). The correction function g_ω is adopted according to [32], i.e.:

$$g_\omega = \frac{\rho_{ws}^l}{\rho_w^l} (1 - 0.03m) \tag{15}$$

being m the molality of the solution.

Salt precipitation has an impact on the gas and liquid permeability of the porous medium. This phenomenon is accounted for by updating K_g and K_l through correction functions ($g_g = g_l = 1 - S_s^s$, from [23]) based on the effective porosity ϕ_{eff}:

$$K_g \leftarrow g_g(\phi_{eff}) K_g, \quad K_l \leftarrow g_l(\phi_{eff}) K_l \tag{16}$$

where

$$\phi_{eff} = \phi_0 (1 - S_s^s) \tag{17}$$

The salt diffusion coefficient K_s depends on the salt solution saturation degree S_{ws}^l:

$$K_s \leftarrow K_s \bullet S_{ws}^l \tag{18}$$

In this multiphase model, the salt solution saturation degree S_{ws}^l is written as function of the relative humidity h through the sorption/desorption curve $S_{ws}^l(h)$.

The multiphase model is finally set by the boundary conditions, which can have four forms:

$$h = \overline{h} \tag{19}$$

$$\omega = \overline{\omega} \tag{20}$$

$$\mathbf{j}_w \bullet \mathbf{n} = q_w + \gamma_w (A_w h - h_{env}) \tag{21}$$

$$\mathbf{j}_s^l \bullet \mathbf{n} = q_\omega \tag{22}$$

where $\mathbf{n}$ is the outward unit normal to the boundary, $\overline{h}$ and $\overline{\omega}$ the prescribed humidity and salt concentration, respectively, q_w and q_ω,the prescribed normal fluxes of moisture and salt, respectively, h_{env} the prescribed environmental humidity,A_w the water activity, and γ_w the convective humidity coefficient.

A standard iterative strategy based on the Newton-Raphson method has been applied to solve the non-linear system of differential equations. The time discretization has been performed through the backward finite difference method. This model has been implemented in COMSOL Multiphysics [36] using hexahedral finite elements with quadratic shape functions.

3.2. Model validation and comparison with experimental results

The model validation is herein presented and discussed through the comparison with experimental results. Firstly, the numerical set-up is discussed together with the adopted boundary and initial conditions (Section 3.2.1). Then, a comprehensive comparison with experimental results is shown and discussed to validate the model (Section 3.2.2).

3.2.1. Numerical set-up

The drying phase, presented in Section 2.2, is simulated (Fig. 5) using as initial domain conditions the situation at the end of the wetting phase, i.e. fully saturated stone (h = 100%) with a varying dissolved salt content ($\omega = \omega$) depending on the stone properties. The value of ω is chosen to correspond to a salt content in the specimen of 1 wt% of its dry weight, as considered in the experimental campaign. Accordingly, the value ω = 6.7% is adopted for Migné (MI) while ω = 3.8% is assumed

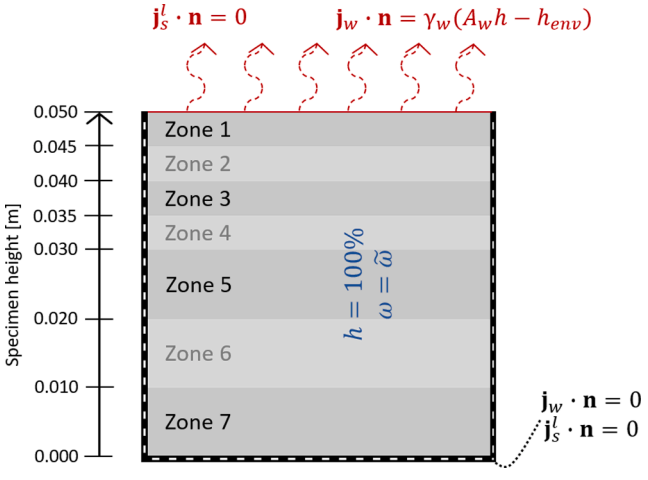

Fig. 5. Boundary and initial conditions, and zones definition.

for Maastricht (MA).

Zero-flux boundary conditions (i.e. $\mathbf{j}_w \cdot \mathbf{n} = 0$ and $\mathbf{j}_s^l \cdot \mathbf{n} = 0$) are considered on the bottom and lateral sides, while on the top surface moisture flux is allowed $\mathbf{j}_w \cdot \mathbf{n} = \gamma_w (A_w h - h_{env})$, h_{env} being the prescribed environmental humidity, equal to 12% (the mean relative humidity measured in the climatic chambers described in section 2.2). For sodium chloride solutions, A_w is equal to 1 when $\omega = 0$ and equal to 0.75 when $\omega = \omega_{sat}$. The convective humidity coefficient γ_w can be considered constant and equal to $\gamma_w = 0.21$ kg/m^2/s [23] when there is no formation of salt crusts on the evaporating surfaces. Conversely, this coefficient can decrease when the pore filling exceeds a certain threshold $\overline{S_s^s}$, following the exponential phenomenological relationship proposed in [23]. This setting is marked in the following with subscript *cr* indicating the hypothesis of crust formation.

Given the axial symmetry of the problem (see Fig. 5 and considering that the specimen is cylindrical) and considering that the whole drying phenomenon only develops along the vertical direction, a thin vertical strip of the domain is extracted and studied. A square cuboid domain of $0.001 \times 0.001 \times 5mm^3$ composed of a single line of 200 hexahedral finite elements is considered, using a mesh bias to ensure refinement on the top of the domain.

A summary of the model parameters for NaCl solutions is given in Table 2. The model parameters for the Maastricht and Migné stone are collected in Table 3. All these parameters have been determined within the experimental campaign discussed in Section 2, as well as the sorption/desorption curves $S_{ws}^l(h)$. Only the vapor permeability D_v was not experimentally investigated. Parametric studies have been carried out varying this property within a realistic range to investigate its influence on the modelling results. The results were found not to be affected by variations in D_v and the realistic values given in Table 3 have been utilized.

3.2.2. Numerical model validation

The first type of results that have been compared are the drying curves. Numerical and experimental drying curves with pure water and with salt solutions are shown in Fig. 6 for Migné and Maastricht limestone. The water content in the numerical simulations is computed through:

$$\text{Water content (wt.\%)} = \frac{\int_V S_{ws}^l(h)\phi_0\rho_w^l}{\int_V \rho_m} \tag{23}$$

V being the volume of the integration, in this case equal to the whole specimen volume. As can be noted in Fig. 6, the numerical and experimental drying curves with pure water are in good agreement for both stones. Indeed, numerical curves appear reasonably included within the standard deviation of the experimental curves. Additionally, the initial water content, i.e. the condition at the beginning of the drying phase, is effectively represented in the numerical simulations.

A good agreement also arises from the Migné drying curves with salt solution (Fig. 6a), where the drying is evidently slower than the case with pure water. It should be pointed out that the influence of the hypothesis of crust formation (*num_NaCl_cr*, Fig. 6a) in the numerical drying curves appears moderate (the drying is slightly slower than the case without crust formation hypothesis (*num_NaCl*, Fig. 6a)). Both numerical curves appear included within the experimental range, with the experimental curves, obtained in different laboratories, being very similar.

Conversely, the experimental curves obtained in the two different laboratories for drying with salt solution show significant differences for Maastricht (compare *exp1_NaCl* with *exp2_NaCl*, Fig. 6b). Here, the influence of the hypothesis of crust formation in the numerical drying curves is much more significant than for the Migné case. A good agreement can be noted between the numerical drying curve without crust formation *num_NaCl* and the *exp1_NaCl* curve. The numerical curve with crust formation *num_NaCl_cr* shows a good agreement with the *exp2_NaCl* curve, which has a significantly slower drying behavior.

The second type of results that have been compared concerns the crystallized salt distribution within the stones. The numerical crystallized salt c_s^s and pore filling S_s^s profiles are given in Fig. 7. The salt accumulation up to 1 mm depth as experimentally observed [18] is numerically well-reproduced.

This aspect is even more clear by inspecting Fig. 8, where the numerical c_s^s and pore filling profiles are shown for the first upper 5 mm. Indeed, the pore filling reaches significant values (more than 95% for Migné and more than 75% for Maastricht) in the very top part of the specimen, and it decreases sharply within 1–1.5 mm from the top up to negligible values. Fig. 8 shows that the influence of crust formation on the pore filling profile is moderate for both stones. Thus, the possibility of accumulating solid salt in a thin upper layer at the end of the contamination procedure does not appear particularly influenced by the potential salt crust formation on the top surface.

For the sake of comparison, the relative adimensional drilling force profiles obtained through the drilling resistance method (DRMS) are also shown in Fig. 8. A post-processing of the DRMS results [18] has been carried out with the aim of further qualitatively comparing numerical and experimental data. Therefore, the drilling force profiles obtained on pure water-contaminated stones have been subtracted from the drilling force profiles obtained on salt-contaminated stones. The resulting profiles have then been normalized to the maximum force to obtain a qualitative profile indicating the presence of crystallized salt. A reasonably good agreement is again obtained by comparing these profiles with the numerical pore filling profiles. Indeed, they both show that the crystallized salt layer arises in the very upper part of the specimen.

The third type of results that were compared concerns the salt content in the various zones of the specimen (see Fig. 5 for zones definition). The salt content in Migné and Maastricht specimens is shown in Fig. 9 and Fig. 10, respectively. Both figures show the numerical crystallized/dissolved/total salt content time-histories in each zone of the specimen. These quantities are computed as follows:

$$\text{Crystallized NaCl (wt.\%)} = \frac{\int_V c_s^s}{\int_V \rho_m} \tag{24}$$

Table 2
Summary of the model parameters for NaCl solution.

	Quantity	Value	Source
K_c	Growth rate coefficient	0.03 μm/s	Refs. [37,38]
n	Nuclei in solution	$4 \cdot 10^{-6}$ (μm^3)$^{-1}$	Ref. [39]
P	Crystallization process order	1	Ref. [23,40]
ω_{sat}	Concentration of dissolved NaCl at saturation	0.264 kg/kg	Literature
α_0	Crystallization threshold	1	Ref. [39]
K_s	Salt diffusion coefficient	$1.5 \cdot 10^{-9}$ m^2/s	Ref [41]
ρ_s^s	Solid NaCl density	2160 kg/m^3	Literature

Table 3
Model parameters for Maastricht and Migné limestone.

	Quantity	Maastricht	Migné
ϕ_0	Capillary active porosity	42.0%	27.3%
ρ_m	Stone density	1270 kg/m^3	1819 kg/m^3
A_{cap}	Capillary absorption coeff.	22.21 kg/m^2/min$^{0.5}$	2.31 kg/m^2/min$^{0.5}$
F_1	Water diffusivity coeff.	0.28	0.60
F_2	Water diffusivity coeff.	1.69	1.68
D_v	Vapor diffusivity	$2.2 \cdot 10^{-5}$ m^2/s	$2.6 \cdot 10^{-7}$ m^2/s
r_p	Mean pore radius	15 μm	0.47 μm

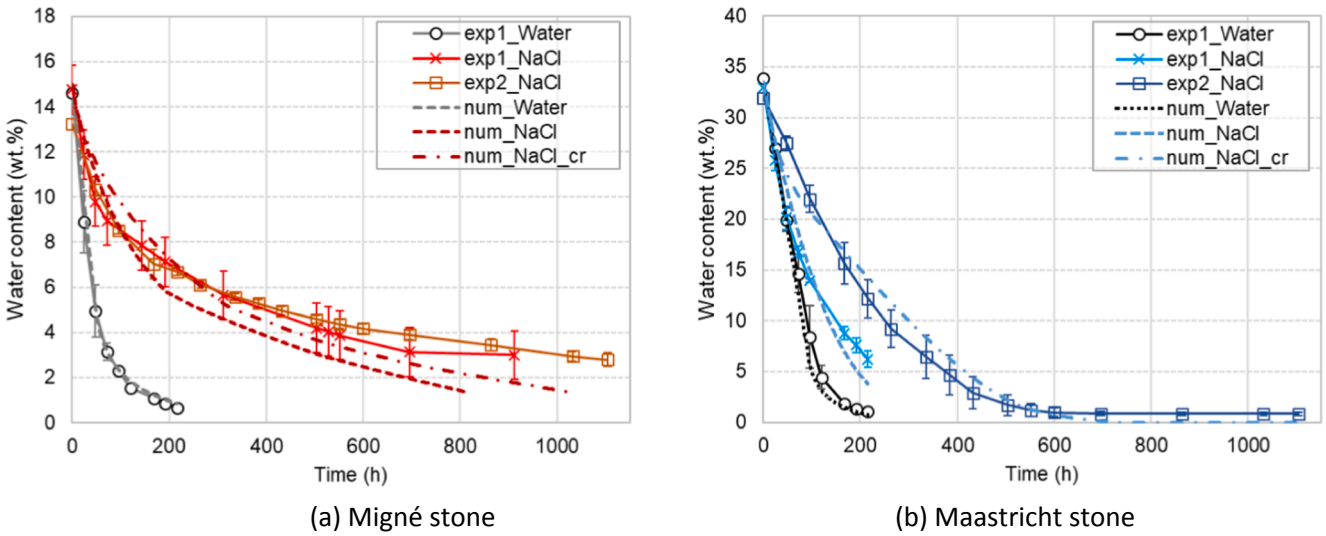

Fig. 6. Drying curves for Maastricht and Migné stone obtained experimentally and predicted numerically.

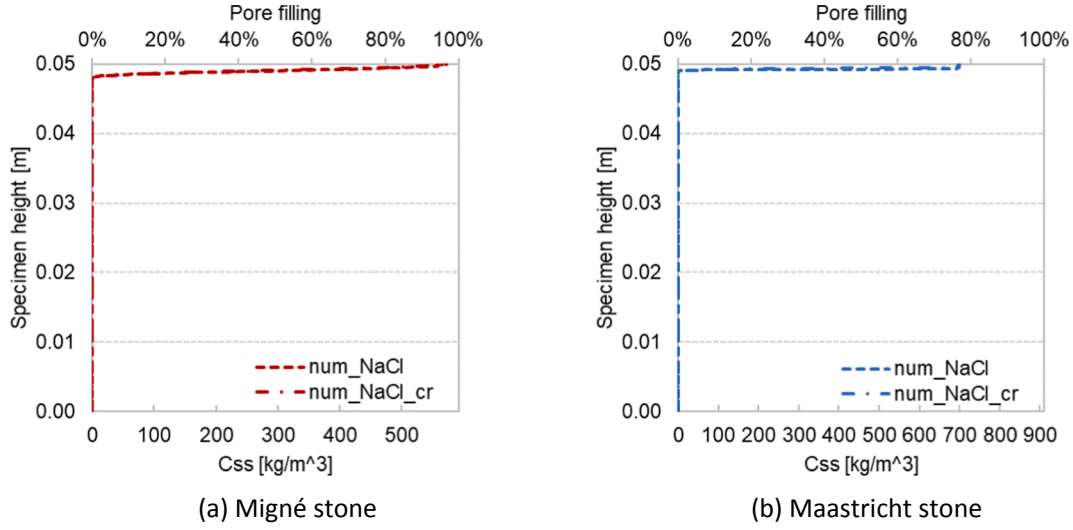

Fig. 7. Crystallized salt distribution in (a) Maastricht and (b) Migné limestone, as predicted numerically after decreasing the water content by 85%.

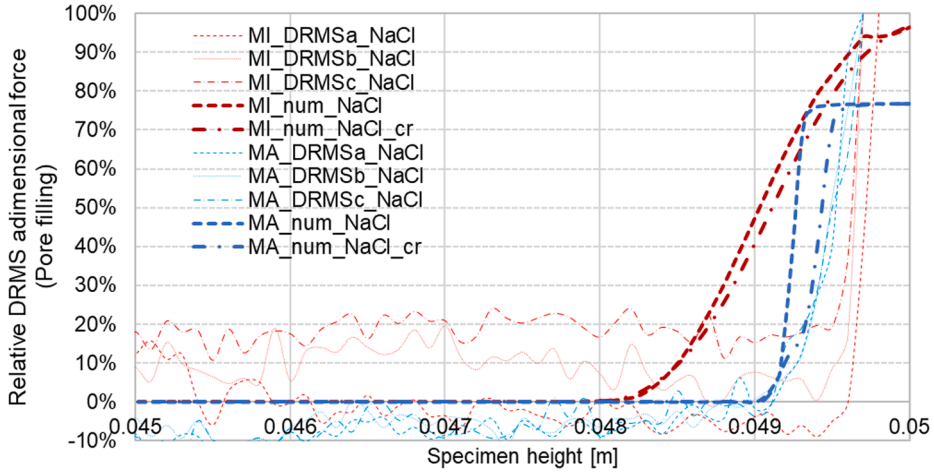

Fig. 8. Relative DRMS adimensional force versus numerical pore filling in the top 5 mm of the specimen (MI-Migné, MA-Maastricht).

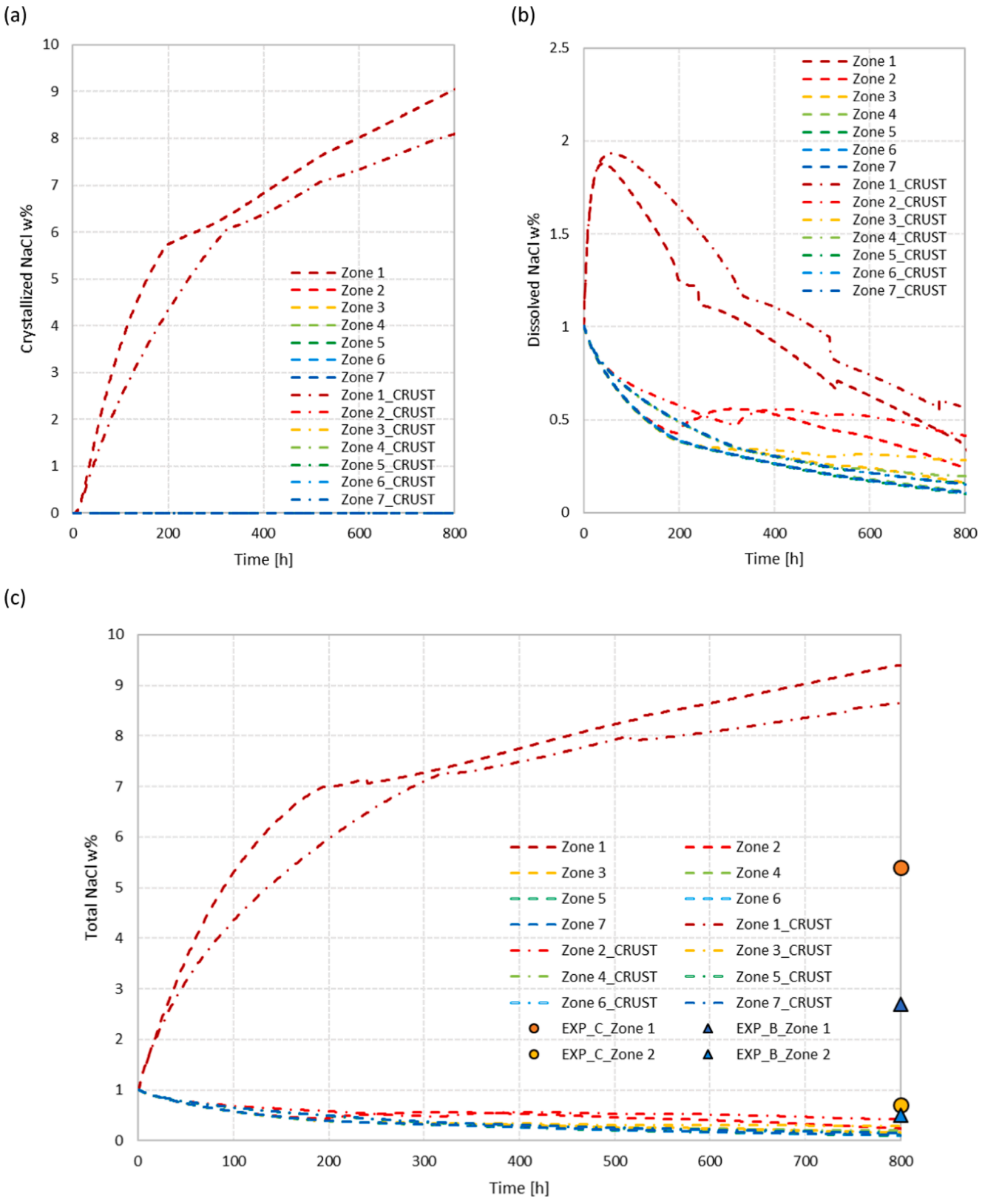

Fig. 9. Salt content in the seven zones (see Fig. 5) of the Migné specimen: (a) numerical crystallized salt, (b) numerical dissolved salt, and (c) numerical total amount of salt compared with experimental data at the end of the weathering procedure.

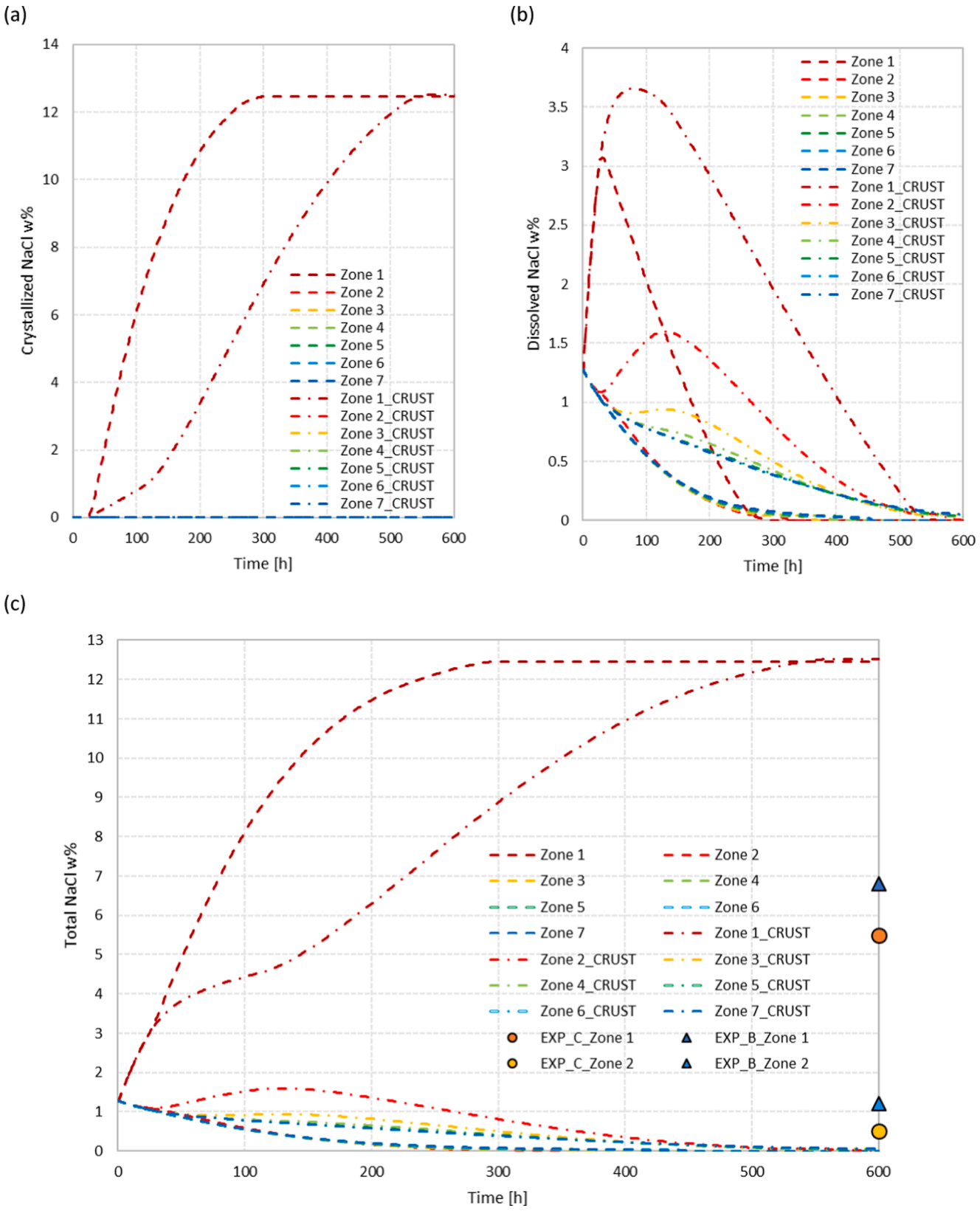

Fig. 10. Salt content in the seven zones (see Fig. 5) of the Maastricht specimen: (a) numerical crystallized salt, (b) numerical dissolved salt, and (c) numerical total amount of salt compared with experimental data at the end of the weathering procedure.

$$\text{Dissolved NaCl (wt.\%)} = \frac{\int_V \omega \; S_{ws}^{l}(h)\phi_0\rho_{ws}^{l}}{\int_V \rho_m} \tag{25}$$

$$\text{Total NaCl (wt.\%)} = \text{Crystallized NaCl (wt.\%)} + \text{Dissolved NaCl (wt.\%)} \tag{26}$$

Here, the volume of the integration V equals the volume of the zone analysed.

As can be noted in Fig. 9a and Fig. 10a, significant salt crystallization only occurs in Zone 1 (i.e. the top zone, Fig. 5) for both stones. The evolution of crystallized NaCl is not significantly influenced by the formation of crust for Migné (Fig. 9a), whereas the accumulation of solid NaCl in Zone 1 is significantly delayed by the formation of crust for Maastricht (Fig. 10a).

Concerning the dissolved NaCl content time-history in the stones (Fig. 9b and Fig. 10b), although all zones have initially the same content, dissolved salt increases in the first hours in Zone 1 while decreasing in all the other zones. This indicates that the dissolved salt transport moves towards the top surface, where evaporation is allowed. After a certain amount of time (within 20 h and 100 h), also the dissolved salt content in Zone 1 starts decreasing, suggesting that the salt is precipitating, crystallizing close to the top.

In Fig. 9c and Fig. 10c, the numerical total amount of salt for both stones is compared with experimental data at the end of the weathering procedure using ion chromatography results [18]. Only the ion chromatography-measured salt content related to Zone 1 and Zone 2 are reported, as the salt content measured in the other zones appears very close to zero. The values reported are the mean value of three different measurements.

Focusing the attention on Zone 1 (as in Zone 2 the salt content is already very low), a significant scattering of experimental results can be observed (this is the clearest for Migné where the measurement for *exp1* is about double of the measurement for *exp2*). For both stones, the numerical total NaCl content at the end of the simulation is significantly greater than the experimental values, although they show the same order of magnitude. This outcome was somehow expected due to the following two reasons:

1) The model supposes no flux of dissolved salt on the top surface ($\mathbf{j}_s^l \bullet \mathbf{n} = 0$), i.e. salt mass does not change within the domain. Conversely, salt efflorescence was experimentally observed [18] and this phenomenon certainly can reduce the NaCl content in the top zone. So, an overestimation of the numerical NaCl contents with respect to the experimental values is expected in Zone 1.
2) The crystallized salt c_s^s is averaged on the whole volume of Zone 1, see (24). However, as can be noted in Fig. 7, the crystallized salt presents a huge gradient in the top part of Zone 1. Accordingly, a slight variation of the position of extraction of the fragment for ion chromatography (e.g. 1 mm) could potentially influence the experimental measures significantly.

4. Predicting salt accumulation in natural building stones for the RILEM ASC-271 accumulation procedure

4.1. Numerical results for different stones

In order to illustrate the general applicability of our numerical model and of the salt accumulation procedure, we apply it for assessing NaCl accumulation in two other types of stone, namely Tuffeau limestone (TU) and Prague sandstone (PR). Tuffeau limestone has pore diameters ranging from 10 nm up to 100 μm, whereas Prague sandstone has a unimodal pore size distribution. The stone properties have been reported by Beck et al. [27] for Tuffeau limestone, and by Pavlik et al. [42] and Desarnaud et al. [34] for Prague sandstone (Msené sandstone). The physical and moisture properties as used in the simulations are summarized in Table 4. Note that, with respect to Migné limestone, the capillary absorption coefficient, i.e. a measure for the stone permeability, is twice as large for Tuffeau limestone, and four times as large for Prague sandstone. Maastricht limestone is a real limit case, with a very large absorption coefficient, ten times larger than the one of Migné. Following the same criterion used above, i.e. the stone is initially saturated with a salt solution with concentration of 1 wt% of the stone's dry weight, the value $\omega = 7.4\%$ is adopted for Prague, while $\omega = 3.4\%$ is assumed for Tuffeau.

Table 4
Model parameters for Tuffeau limestone and Prague sandstone.

	Quantity	Tuffeau	Prague
ϕ_0	Capillary active porosity	36.5%	22.7%
ρ_m	Stone density	1300 kg/m^3	1890 kg/m^3
A_{cap}	Capillary absorption coeff.	4.20 kg/m^2/min$^{0.5}$	9.88 kg/m^2/min$^{0.5}$
F_1	Water diffusivity coeff.	1.5	3.8
F_2	Water diffusivity coeff.	3.8	3
D_v	Vapor diffusivity	$1.5 \cdot 10^{-9}$ m^2/s	$1.9 \cdot 10^{-6}$ m^2/s
r_p	Mean pore radius	5 μm	15 μm

Results of the four stones in terms of drying curves, total salt content in Zone 1 and pore filling distribution are collected in Fig. 11 and Fig. 12. As can be noted, similar values of total salt content in Zone 1 as for Migné are observed for Prague and Tuffeau (Fig. 11b). Additionally, the possibility of accumulating solid salt in a thin layer (about 1 mm) in the top of the specimen appears verified in all stones (Fig. 12). This is a positive outcome for the general applicability of the accumulation procedure proposed by the RILEM TC ASC-271.

4.2. Numerical results for different boundary and initial conditions

Here, numerical results obtained by varying boundary and initial conditions on the Migné and Maastricht specimens are presented and discussed. Starting from the set-up described in Section 3 (drying at 12% RH and a salt concentration of $\omega = 6.7\%$ for Migné and $\omega = 3.8\%$ for Maastricht), one condition per simulated case is changed: (1) drying at 50% RH, i.e. $h_{env} = 50\%$ (indicated in the following with the subscript *RH50*), (2) drying at 30% RH, i.e. $h_{env} = 30\%$ (indicated in the following with the subscript *RH30*), and (3) increasing the initial salt concentration to 10 wt%, i.e. $\omega = 10\%$ (indicated in the following with the subscript *omega10*).

Resulting parametric drying curves are collected in Fig. 13a and Fig. 13b for Migné and Maastricht, respectively. By increasing the environmental relative humidity and the initial salt content, the drying is slower, as expected. Especially when drying at 50% RH, the drying and accumulation significantly slow down, as it takes more than double the time to lose the same amount of water, or precipitate the same amount of salt, compared to drying at 12% RH. Results in terms of total salt content in Zone 1 are shown in Fig. 14a and Fig. 14b for Migné and Maastricht, respectively. The final NaCl content in the top part is not particularly affected by the relative humidity at which the sample is dried, whereas higher values of initial salt content produce higher values of NaCl content in the top part. Finally, the profiles of pore filling along the specimen height (top 5 mm) for Migné (Fig. 15a) and Maastricht (Fig. 15b) show that the accumulation of solid salt in a thin top layer does not significantly change by drying at a higher relative humidity, but it enlarges by increasing the salt concentration to 10 wt%, especially for Maastricht for which the concentration was increased with a factor 2.6.

5. Conclusions

We have proven that the employed multiphase numerical model is

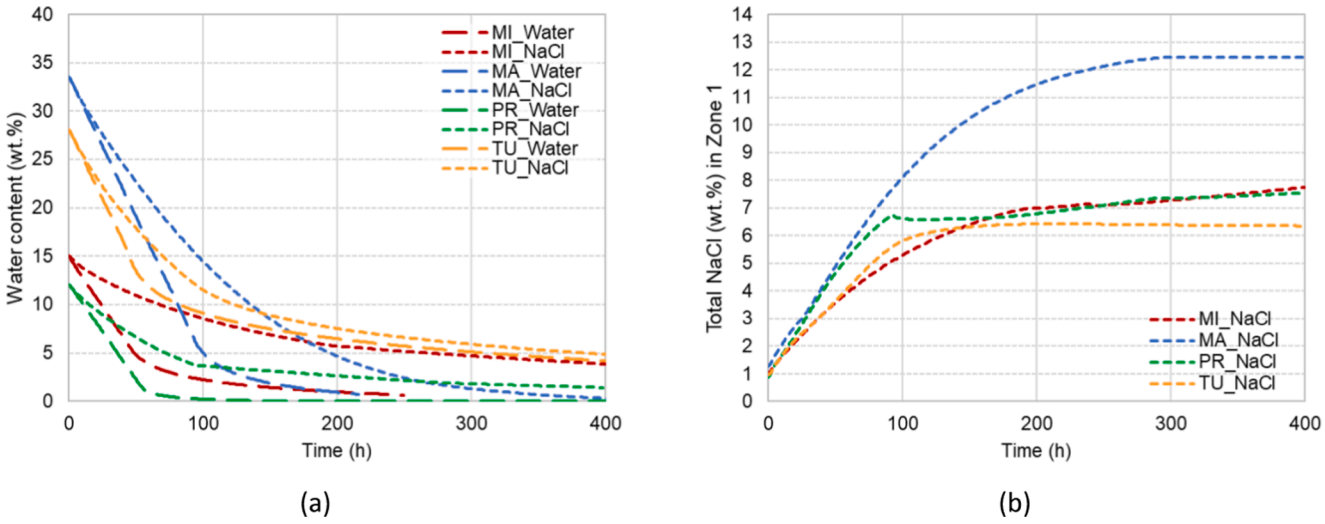

Fig. 11. (a) Drying curves and (b) total salt content in Zone 1 for the four stones (MI-Migné, MA-Maastricht, PR-Prague, TU-Tuffeau).

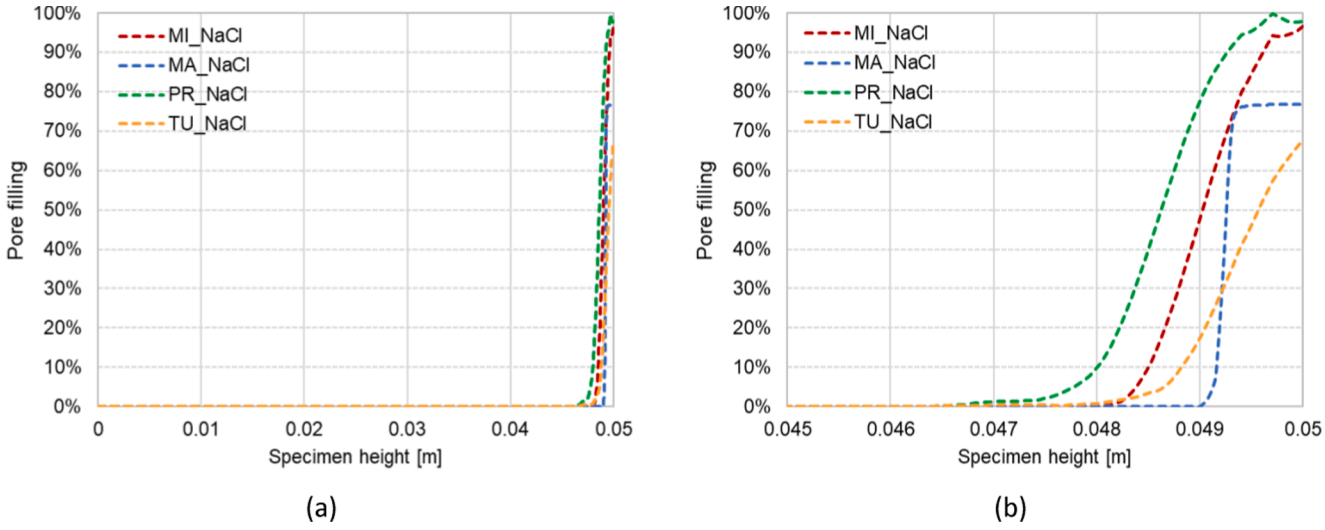

Fig. 12. Pore filling along the specimen height for the four stones: (a) full specimen height, and (b) top 5 mm after 400 h of drying (MI-Migné, MA-Maastricht, PR-Prague, TU-Tuffeau).

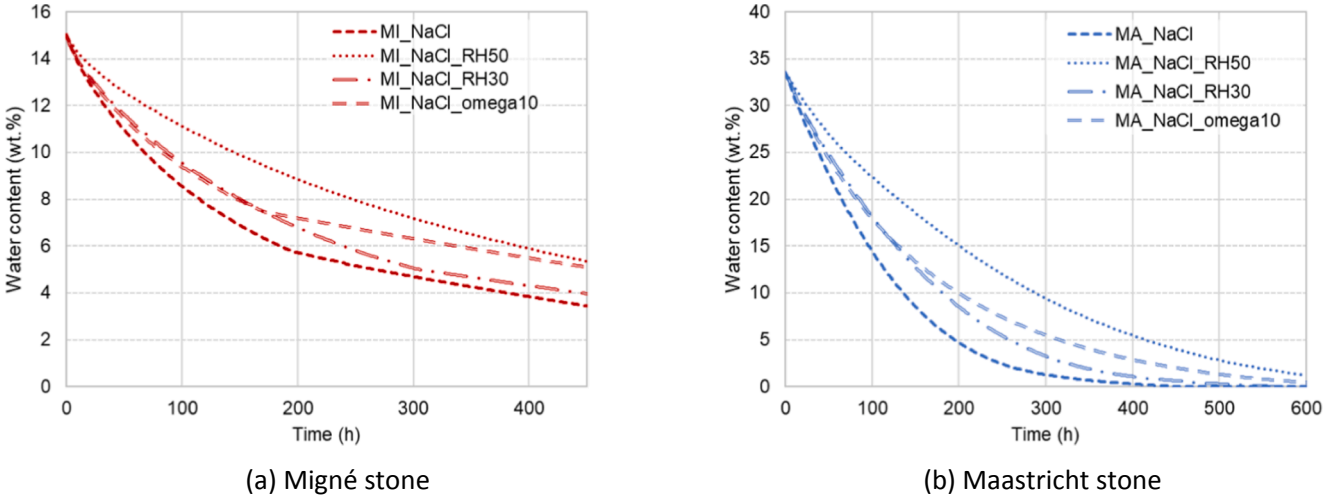

Fig. 13. Drying curves with different boundary and initial conditions for (a) Migné and (b) Maastricht limestone.

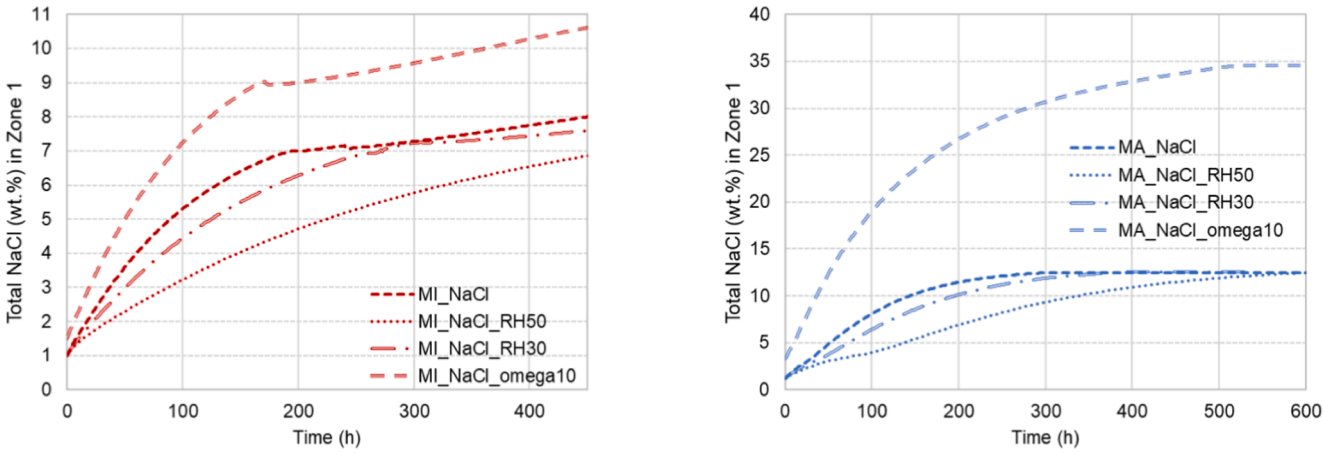

Fig. 14. Total salt content in Zone 1 with different boundary and initial conditions for (a) Migné and (b) Maastricht limestone.

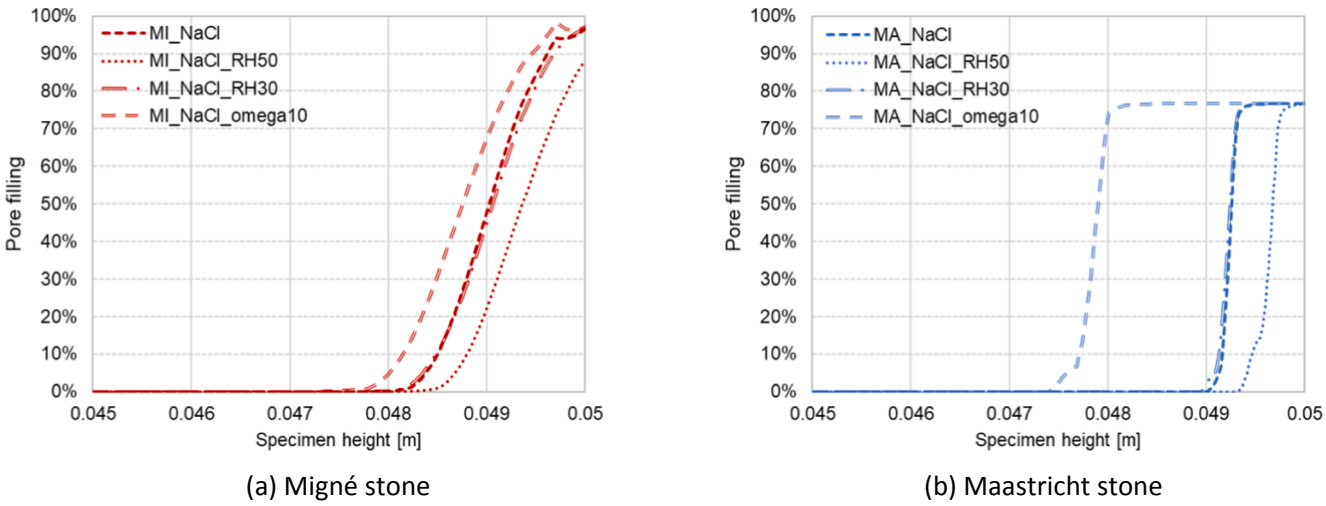

Fig. 15. Pore filling along the specimen height (top 5 mm) for (a) Migné (after 450 h of drying), and (b) Maastricht (after 600 h of drying).

capable of reproducing the salt accumulation procedure proposed by the RILEM TC ASC-271. The model shows to be robust in reproducing the behaviour of the two porous building materials selected by the TC ASC-271 for the experimental development of the procedure, Maastricht and Migné limestone. This implies that it can be used for predicting the salt accumulation behaviour of porous building materials, when the material properties, as listed in Table 3, together with the sorption isotherm, are known. The model focuses on sodium chloride accumulation. The prediction of sodium sulphate accumulation will be the subject of future work, as this requires the implementation and validation of the potential precipitation of the different crystal phases of sodium sulphate.

By numerically reproducing the salt contamination procedure on two other porous stones, Tuffeau limestone and Prague sandstone, we demonstrate that the procedure should be suitable for a range of porous building materials. Both stones accumulate a significant amount of salt in a thin layer close to their top surface, complying with the criterion defined by the TC ASC-271 to create a local zone with a high potential of inducing salt damage once the propagation stage sets in.

Furthermore, the numerical study shows that while the procedure experimentally tested by Nunes et al. [18] consisted in drying at 10% RH, drying up to 30% RH does not significantly impact the drying kinetics nor the salt distribution. Thus even if practitioners do not have access to a climatic chamber allowing for very low humidity, the procedure still holds. Drying at even higher RH will slow down the procedure, but the final salt distribution at the end of drying remains similar. With increasing salt concentration, the salt distributes over a larger thickness close to the top. Therefore, depending on the desired salt thickness prior to the propagation phase, a higher or lower salt concentration could be adopted.

Overall, the numerical modelling predicts that the accumulation procedure is generally applicable. This will be confirmed experimentally by a round robin test. The test is currently ongoing and includes both the accumulation and propagation phase. Nine different porous building materials are tested at eleven different laboratories. The selected materials include Tuffeau limestone and Prague sandstone, along with other natural stones and brick. The TC ASC-271 plans to publish the new salt weathering procedure in 2022. Subsequently, recommendations to standards will be provided.

CRediT authorship contribution statement

Antonio Maria D'Altri: Conceptualization, Methodology, Software, Data curation, Writing – original draft. **Stefano de Miranda:** Conceptualization, Methodology, Writing – review & editing, Supervision. **Kevin Beck:** Methodology, Data curation, Writing – original draft. **Tim De Kock:** Methodology, Writing – review & editing. **Hannelore Derluyn:** Conceptualization, Methodology, Data curation, Writing – original draft, Writing – review & editing, Supervision.

Declaration of Competing Interest

The authors declare that they have no known competing financial interests or personal relationships that could have appeared to influence the work reported in this paper.

Acknowledgement

All authors acknowledge Cristiana Nunes and Beatriz Menendez for providing the drying curves acquired during their salt accumulation procedure, and thank Cristiana Nunes for reading and giving helpful comments on the paper. The authors also thank all other members of the RILEM TC-ASC-271 for their contribution in the discussions leading to this publication.

A.M. D'Altri and S. de Miranda acknowledge the support from the European project CRYSTINART through the Joint Programming Initiative on Cultural Heritage (JPI-CH). T. De Kock was a postdoctoral fellow of the Research Foundation – Flanders (FWO) at the time of the experiments and wants to acknowledge its support. H. Derluyn acknowledges the support from the European Research Council (ERC) under the European Union's Horizon 2020 research and innovation programme (grant agreement N° 850853).

References

[1] A.E. Charola, Salts in the deterioration of porous materials: an overview, J. Am. Inst. Conserv 39 (3) (2000) 327–343.
[2] F.F.M. Filho, H. Morillas, H. Derluyn, M. Maguregui, D. Grégoire, In-situ versus laboratory characterization of historical site in marine environment using X-ray fluorescence and Raman spectroscopy, Microchem. J. 147 (2019) 905–913.
[3] A.M. D'Altri, S. de Miranda, Environmentally-induced loss of performance in FRP strengthening systems bonded to full-scale masonry structures, Constr. Build. Mater. 249 (2020), 118757.
[4] B. Lubelli, V. Cnudde, T. Diaz-Goncalves, E. Franzoni, R. van Hees, I. Ioannou, B. Menendez, C. Nunes, H. Siedel, M. Stefanidou, V. Verges-Belmin, H. Viles, Towards a more effective and reliable salt crystallization test for porous building materials: state of the art, Mater. Struct. 51 (2018) 55.
[5] R. Flatt, N. Mohamed, F. Caruso, H. Derluyn, J. Desarnaud, B. Lubelli, R. Espinosa-Marzal, L. Pel, C. Rodriguez-Navarro, G. Scherer, N. Shahidzadeh, M. Steiger, Predicting salt damage in practice: a theoretical insight into laboratory tests, RILEM Tech. Lett. 2 (2017) 108–118.
[6] R.J. Flatt, Salt damage in porous materials: how high supersaturations are generated, J. Cryst. Growth 242 (3-4) (2002) 435–454.
[7] G.W. Scherer, Stress from crystallization of salt, Cem. Concr. Res. 34 (9) (2004) 1613–1624.
[8] M. Steiger, Crystal growth in porous materials—I: The crystallization pressure of large crystals, J. Cryst. Growth 282 (3-4) (2005) 455–469.
[9] M. Steiger, Crystal growth in porous materials—II: Influence of crystal size on the crystallization pressure, J. Cryst. Growth 282 (3-4) (2005) 470–481.
[10] ASTM B117–03, "Standard practice for operating salt spray (fog) apparatus," 2003.
[11] CEN EN 14147, "Natural stone test methods - Determination of resistance to ageing by salt mist," 2003.
[12] D. Benavente, M. del Cura, J. Garcıa-Guinea, S. Sánchez-Moral, S. Ordóñez, Role of pore structure in salt crystallisation in unsaturated porous stone, J. Cryst. Growth 260 (3–4) (2004) 532–544.
[13] S. Yu, C.T. Oguchi, Role of pore size distribution in salt uptake, damage, and predicting salt susceptibility of eight types of Japanese building stones, Eng. Geol. 115 (3-4) (2010) 226–236.
[14] M. Angeli, J.-P. Bigas, D. Benavente, B. Menéndez, R. Hébert, C. David, Salt crystallization in pores: quantification and estimation of damage, Environ. Geol. 52 (2) (2007) 205–213.
[15] A. Zalooli, D. Freire-Lista, M. Khamehchiyan, M. Nikudel, R. Fort, S. Ghasemi, Ghaleh-khargushi rhyodacite and Gorid andesite from Iran: characterization, uses, and durability, Environ. Earth Sci. 77 (8) (2018) 315.
[16] D. Benavente, J. Martínez-Martínez, N. Cueto, M.A. García-del-Cura, Salt weathering in dual-porosity building dolostones, Eng. Geol. 94 (3-4) (2007) 215–226.
[17] E. Doehne, "Salt weathering: a selective review," Geological Society Special Publication, vol. 205, no. 51-64, 2002.
[18] C. Nunes, A. Aguilar Sanchez, S. Godts, D. Gulotta, I. Ioannou, B. Lubelli, B. Menendez, N. Shahidzadeh, Z. Slizkova, M. Theodoridou, Experimental research on salt contamination procedures and methods for assessment of the salt distribution, Constr. Build. Mater. 298 (2021) 123862.
[19] H. Derluyn, P. Moonen, J. Carmeliet, Deformation and damage due to drying-induced salt crystallization in porous limestone, J. Mech. Phys. Solids 63 (2014) 242–255.
[20] M. Koniorczyk, Modelling the phase change of salt dissolved in pore water - Equilibrium and non-equilibrium approach, Constr. Build. Mater. 24 (7) (2010) 1119–1128.
[21] M. Koniorczyk, D. Gawin, Modelling of salt crystallization in building materials with microstructure – Poromechanical approach, Constr. Build. Mater. 36 (2012) 860–873.
[22] G. Castellazzi, C. Colla, S. de Miranda, G. Formica, E. Gabrielli, L. Molari, F. Ubertini, A coupled multiphase model for hygrothermal analysis of masonry structures and prediction of stress induced by salt crystallization, Constr. Build. Mater. 41 (2013) 717–731.
[23] L. Grementieri, L. Molari, H. Derluyn, J. Desarnaud, V. Cnudde, N. Shahidzadeh, S. de Miranda, Numerical simulation of salt transport and crystallization in drying Prague sandstone using an experimentally consistent multiphase model, Build. Environ. 123 (2017) 289–298.
[24] Standard EN 1925 (B10-613), "Test methods for natural stones - Determination of the coefficient of water absoprtion by capillarity," 1999.
[25] Standard NF P94-420, "Rocks - Determination of the uniaxial compressive strength," 2000.
[26] Standard NF P94-422, "Rocks - Determination of tensile strength by an indirect method - Brazilian test," 2001.
[27] K. Beck, M. Al-Mukhtar, O. Rozenbaum, M. Rautureau, Characterization, water transfer properties and deterioration in tuffeau: building material in the Loire valley—France, Build. Environ. 38 (9–10) (2003) 1151–1162.
[28] S. Siegesmund, H. Dürrast, in: Stone in Architecture, Springer Berlin Heidelberg, Berlin, Heidelberg, 2011, pp. 97–225.
[29] J. Carmeliet, H. Hens, S. Roels, O. Adan, H. Brocken, R. Cerny, Z. Pavlik, C. Hall, K. Kumaran, L. Pel, Determination of the liquid water diffusivity from transient moisture transfer experiments, Journal of the Thermal Envelope and Building Science 27 (4) (2004) 277–305.
[30] S. Roels, J. Carmeliet, H. Hens, O. Adan, H. Brocken, R. Cerny, Z. Pavlik, A.T. Ellis, C. Hall, K. Kumaran, L. Pel, R. Plagge, A comparison of different techniques to quantify moisture content profiles in porous building materials, J. Therm. Envel. Build. Sci. 27 (4) (2004) 261–276.
[31] B. Masschaele, M. Dierick, D. Van Loo, M. Boone, L. Brabant, E. Pauwels, V. Cnudde, L. Van Hoorebeke, HECTOR: A 240kV micro-CT setup optimized for research, J. Therm. Envel. Build. Sci. 463 (2013), 012012.
[32] G. Castellazzi, S. de Miranda, L. Grementieri, L. Molari, F. Ubertini, Multiphase model for hygrothermal analysis of porous media with salt crystallization and hydration, Mater. Struct. 49 (3) (2016) 1039–1063.
[33] H. Eloukabi, N. Sghaier, S. Ben Nasrallah, M. Prat, Experimental study of the effect of sodium chloride on drying of porous media: The crusty-patchy efflorescence transition, Int. J. Heat Mass Transf. 56 (1-2) (2013) 80–93.
[34] J. Desarnaud, H. Derluyn, L. Molari, S. de Miranda, V. Cnudde, N. Shahidzadeh, Drying of salt contaminated porous media: Effect of primary and secondary nucleation, J. Appl. Phys. 118 (11) (2015), 114901.
[35] S. Gupta, H.P. Huinink, M. Prat, L. Pel, K. Kopinga, Paradoxical drying of a fired-clay brick due to salt crystallization, Chem. Eng. Sci. 109 (2014) 204–211.
[36] COMSOL multiphysics modeling guide, 2016.
[37] B. Simon, Dissolution rates of NaCl and KCl in aqueous solution, J. Cryst. Growth 52 (1981) 789–794.
[38] N. Shahidzadeh-Bonn, J. Desarnaud, F. Bertrand, X. Chateau, D. Bonn, Damage in porous media due to salt crystallization, Phys. Rev. E 81 (6) (2010).
[39] R.M. Espinosa, L. Franke, G. Deckelmann, Phase changes of salts in porous materials: crystallization, hydration and deliquescence, Constr. Build. Mater. 22 (8) (2008) 1758–1773.
[40] S. de Miranda, A.M. D'Altri, G. Castellazzi, Modeling environmental ageing in masonry strengthened with composites, Eng. Struct. 201 (2019), 109773.
[41] J.A. Rard, D.G. Miller, The mutual diffusion coefficients of NaCl– H 2 O and CaCl 2– H 2 O at 25° C from Rayleigh interferometry, J. Solution Chem. 8 (10) (1979) 701–716.
[42] Z. Pavlík, P. Michálek, M. Pavlíková, I. Kopecká, I. Maxová, R. Černý, Water and salt transport and storage properties of Mšené sandstone, Constr. Build. Mater. 22 (8) (2008) 1736–1748.